Three-dimensional characterization of fatigue-relevant intermetallic particles in high-strength aluminium alloys using synchrotron X-ray nanotomography

E. Nizery, H. Proudhon, J.-Y. Buffiere, P. Cloetens, T.F. Morgeneyer & S. Forest

Published online: 02 Sep 2015.

Submit your article to this journal

Article views: 27

View related articles

View Crossmark data

Taylor & Francis
Taylor & Francis Group

Three-dimensional characterization of fatigue-relevant intermetallic particles in high-strength aluminium alloys using synchrotron X-ray nanotomography

E. Nizery[abc*], H. Proudhon[a], J.-Y. Buffiere[b], P. Cloetens[d], T.F. Morgeneyer[a] and S. Forest[a]

[a] *MINES ParisTech, PSL - Research University, MAT - Centre des Matériaux, CNRS UMR 7633, BP 87, 91 003 Evry, France;* [b] *Université de Lyon, MATEIS, CNRS UMR 5510, 69 621 Villeurbanne Cedex, France;* [c] *Constellium Technology Center, BP27, 38341 Voreppe Cedex, France;* [d] *European Synchrotron Radiation Facility, BP 220, 38 043 Grenoble Cedex, France*

Second-phase particles and small porosities are known to favour fatigue crack initiation in high-strength aluminium alloys 2050-T8 and 7050-T7451. Using high-resolution X-ray tomography (320 nm voxel size), with Paganin reconstruction algorithms, the probability that large clusters of particles contain porosities could be measured for the first time in 3D, as well as precise 3D size distributions. Additional holotomography imaging provided improved spatial resolution (50 nm voxel size), allowing to estimate the probability of finding cracked particles in the as-received material state. The extremely precise 3D shape (including cracks) as well as local chemistry of the particles has been determined. This experiment enabled unprecedented 3D identification of detrimental stress risers relevant for fatigue in as-received aluminium alloys.

Keywords: aluminium alloys; intermetallics; X-ray tomography; 3D characterization; fatigue crack initiation

1. Introduction

Intermetallic particles are known to play a key role during the fatigue crack initiation period in structural aluminium alloys [1–4]. Typical dimensions of the particles observed in rolling direction - transverse direction (RD-TD) plane are in the range $1 - 20\,\mu m$. Their two-dimensional (2D) size distribution has been shown to have a major effect on fatigue life [3,5,6]. However, fatigue crack initiation is a three-dimensional (3D) mechanism for which dimensions of particles in the third dimension is important [7]. Focused ion beam (FIB) is a destructive and time-consuming technique, dedicated to small volumes typically $(10\,\mu m)^3$, which is not appropriate for obtaining a statistically 3D representative distribution. Previous studies using X-ray tomography were performed with a voxel size of $0.7\,\mu m$, which already provided good estimate of size distribution [8], although with such a resolution the exact shape cannot be resolved precisely. This prevents the determination of precise stress concentration which may be a key parameter for fatigue crack initiation.

---

*Corresponding author. Email: erembert.nizery@mines-paris.org

Table 1. Chemical composition (wt%) of the studied plates.

	%Cu	%Zn	%Li	%Mg	%Mn	%Ag	%Zr	%Si	%Fe
2050-T8	3.2-3.9	<0.25	0.7–1.3	0.2–0.6	0.2–0.5	0.2–0.7	0.06–0.14	<0.08	<0.1
7050-T74	2.0–2.6	5.7–6.7	–	1.9–2.6	<0.1	–	0.08–0.15	<0.12	<0.15

In the last years, several materials science studies utilized X-ray tomography with micrometer like resolution to get an insight on the 3D role of the microstructure on mechanical behaviours. Studies were led e.g. on titanium alloys [9], magnesium [10], aluminium alloys [11] and polymers [12]. Developments in magnified holotomography at the European Synchrotron Radiation Facility (ESRF) makes it possible to perform 3D imaging of these particles and porosities, with a resolution as low as 50 nm [13], which allows to detect cracked particles [14]. Holotomography was already used on a AlMg7.3Si3.5 aluminium alloy by Tolnai et al. [15] to study the effect of solution heat treatment.

High- and nanoresolution tomography is thus expected to provide new information relevant to fatigue crack initiation in aluminium alloys. This paper aims at extracting this information for alloys 2050-T8 and 7050-T7451 using improved voxel sizes of 320 nm and 50 nm, respectively. Materials and methods are first introduced, then results obtained, respectively, with high- and nanoresolution tomography are separately presented and finally discussed.

2. Materials and methods

2.1. *Materials*

Plates of rolled aluminium alloys 2050-T8 and 7050-T7451 of thickness 60 mm and 65 mm, respectively, were provided by Constellium for this study. Table 1 gives the material chemical compositions. Both materials contain particles formed during casting process and further deformed during thermomechanical heat treatments. Due to this complex history, the second phase particles end up with a very intricate shape and composition, and are known to influence the fatigue life. A 2D scanning electron microscope (SEM) and energy dispersive X-ray spectroscopy (EDX) characterizations have been conducted on particles of both plates. Among the few tens of particles analysed in the 2050-T8 plate, only Al–Cu–Fe–Mn were detected. They are divided into Cu-rich and Mn-rich phases, also observed by Ma et al. [16] in a 2099-T8 plate. The plate in 7050-T7451 contains only Al_7Cu_2Fe and Mg_2Si particles, which is consistent with those usually reported in the literature for such Al-Zn alloys [17,18]. Typical dimension for the larger particles in RD-TD plane is around 20 μm equivalent diameter. Cavities of a few microns are also detected. Low-stress concentration specimens aligned with the rolling direction from plate in 2050-T8 show improved fatigue lifetime compared to those from plate in 7050-T7451.

2.2. *Data acquisition*

Both high- and nanoresolution imaging of particles and porosities in the two alloys were conducted on the nanoimaging end station of beamline ID22 NI (ESRF, Grenoble). A

monochromatic X-rays beam at 29.6 keV was used. Pixel size for nanoresolution holo-tomography (resp. high-resolution tomography) was 50 nm (resp. 320 nm) (Figure 1). The detector on beamline ID22 is composed of a CCD camera with a 2048 × 2048 pixels area. The total volume analysed is thus a cylinder of 102.4 μm diameter and 102.4 μm height (resp. 655.4 μm). For holotomography, the procedure to achieve reconstruction of phase contrast requires four scans (each one composed of 2000 radiographs). These scans are acquired at four distances between the specimen and CCD detector.

High- and nanoresolution images have been performed on one 2050-T8 Al-alloy and one 7050-T7451 Al-alloy specimen. Both have z-direction aligned with rolling direction (RD). Cylindrical 0.6 mm diameter specimens were cut at 1/4 thickness for the tomographic inspection.

Given the typical size, the volume fraction and the spatial repartition of particles, the nanoresolution imaging of a random zone would, in most cases, fail to contain a dense particle-bearing zone. To centre the high-resolution scans on a particular zone containing particles, the following method apparented to zoom tomography [13] has been used:

- a single high-resolution scan is performed (655 μm containing several hundreds of particles > 10 μm),
- a few slices are reconstructed.
- the displacement of the specimen is carefully calculated to align the chosen zone with beam and rotation axis.
- nanotomography imaging is then carried out.

A quick overview of the experiment is shown in Figure 1.

2.3. *Methods for high-resolution data analysis*

2.3.1. *From 3D size distribution to 2D equivalent diameter*

Reconstructed 32 bit images with voxel size 320 nm are first converted to 8 bit using the following bounds: -436 to 406 for Al2050 and −457 to 457 for Al7050. Voids, particles and matrix are then segmented using grey level thresholding. For the plate in 2050-T8, all particles are considered to be Al–Cu–Fe–Mn (the only particles detected by EDX analysis in Section 2.1). For the plate in 7050-T7451, particles darker than the matrix (inversed colours) contain elements heavier than the matrix, and correspond therefore to Al_7Cu_2Fe. On the contrary, the brighter particles correspond to Mg_2Si. In-house ImageJ plugins are then used to label and compute the 3D size distributions. The equivalent ellipsoid of particles larger than 10 microns and all voids larger than 2 microns are also determined [19].

One of the goals of this work is to evaluate possible errors in terms of particle and void size distributions from surface inspections. Two-dimensional (2D) and three-dimensional (3D) particle equivalent diameter distributions will not have the same physical units (number of particles per mm^2 and per mm^3, respectively). Some tools have been used in the literature to overcome this limitation [20–22], and stereology [23] provided a framework to transform 2D distributions into 3D ones based on the knowledge of 3D shapes. In this paper, we propose an alternative method to transform 3D data into 2D distributions.

For a given material, two different methods are used and compared to provide a 2D distribution from 3D data.
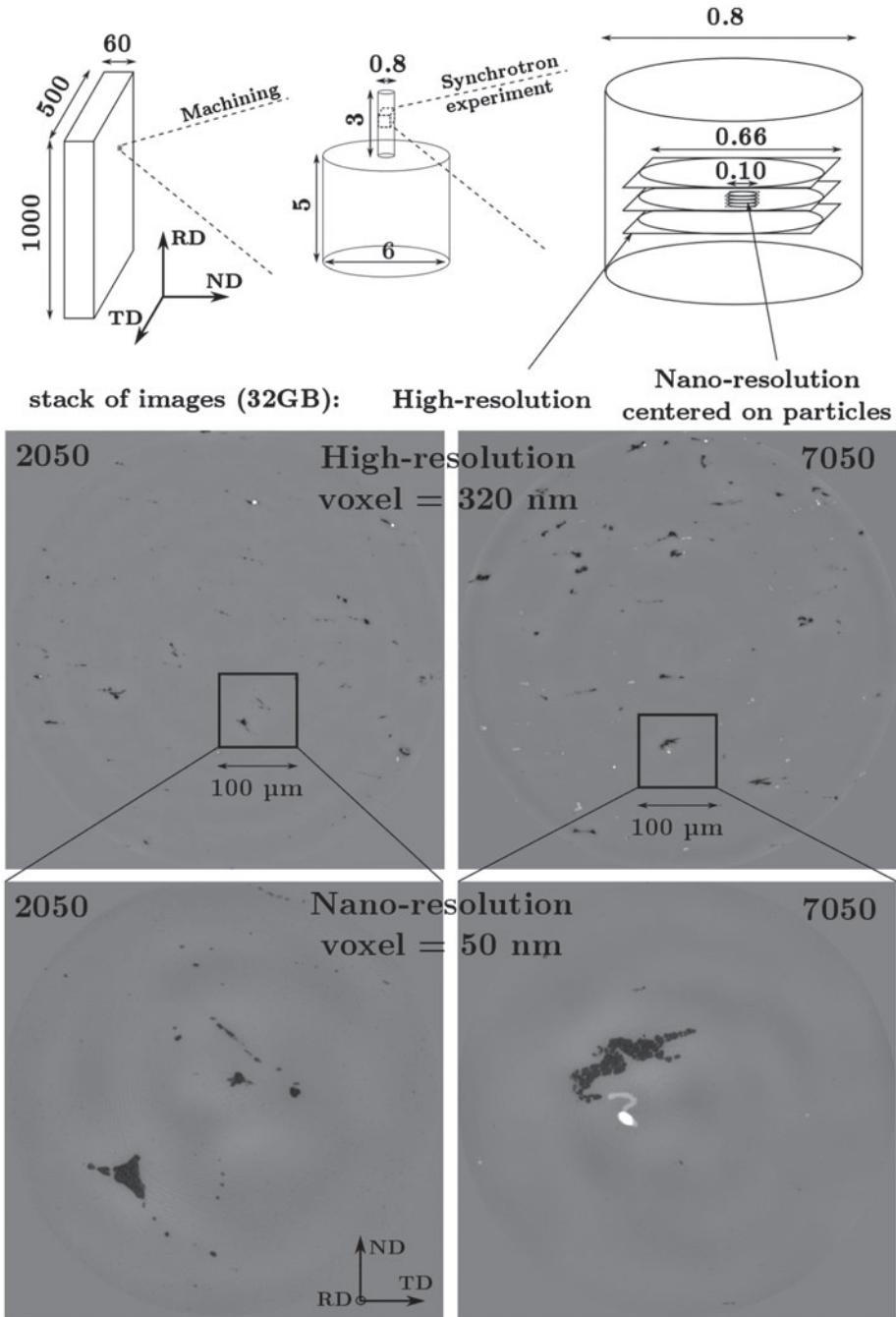
Figure 1. (a) Quick overview from process leading to nanoresolution images from an industrial plate (dimensions in mm), (b) 320 nm-resolution and 50 nm-resolution images from particles contained in 2050-T8 and 7050-T7451 plates (colours are inversed compared to SEM images and classical tomography: particles are in dark).

(1) The first method (which is equivalent to observing a polished surface, called here 'real') consist in analysing size distribution in many RD-TD planes of the 3D-labelled images.

(2) The second method (called here 'ideal') assumes that we cut many slices through a volume, where each particle has been replaced by its equivalent ellipsoid with parameters a, b and c. The particles are assumed to be aligned with the rolling direction RD, as observed for both alloys.

For both methods, 2000 slices have been analysed which correspond to the full 3D stack and to a total surface of 690 mm^2. For each slice, 2D equivalent diameters of particles present in this slice (intersected) are computed. Note that with the first method, a particle with a non-convex shape may lead to several islands on the slice cut through the volume and thus to several equivalent diameter.

2.3.2. *Particles and void clusters*

In this study, a cluster is defined as a set of particles and porosities composed by elements closer than a distance D (the surface distance is considered). For each tomographic volume, the computation of particles and void surface distances in 3D requires 6 hours using 12 cores and 100 Gb. Then, the clusters are constructed as follows:

(1) Let a set contain one particle or one porosity (not contained in any previously constructed cluster),

(2) every particle or porosity which distance (surface-to-surface) to an element of the set is below D = 0.96 microns (3 voxels) is added to the set,

(3) the previous step is repeated until no element can be further added. The final set constitutes a new cluster.

2.4. *Methods for 50 nm voxel size magnified holotomography data analysis*

2.4.1. *3D particle shape*

As before, thresholding of particles and porosities is carried out on holotomography 3D images. The surfaces used for precise 3D morphology visualization, are obtained with Avizo software. Fractured particles are detected with magnified holotomography. Fractures have platelet shapes, and can be therefore clearly distinguished from spherical porosities.

2.4.2. *Local particle density*

In tomography, when phase-contrast reconstructions are used, grey levels are proportional to electron density [24] – number of electrons per unit volume, so that the grey level of a phase can be correlated with the elements that it contains.

In this study, we will assume that electron density is proportional to weight density. In both alloys, void and matrix densities are well known (zero for voids and 2.71 to 2.83 for the Al-matrix, depending on the alloy). Using the letters *d* and *g* for, respectively, densities and grey levels, and remembering that grey levels linearly depend on the electron density

(*i.e.* linearly depend on the weight density in a first approximation), the formula providing the density of an intermetallic particle is then easily obtained with proportionality rules:

$$d_{particle} = \frac{g_{particle} - g_{porosity}}{g_{matrix} - g_{porosity}} \times d_{matrix} \qquad (1)$$

3. High-resolution tomography: results

In this part, results produced by high-resolution tomography are presented: statistical data about size distributions of (i) particles and (ii) porosities and (iii) proximity of particles and porosities.

Contrary to Al–Cu–Fe–Mn particles presented in [8] (classical tomography with voxel size 0.7 μm), the 3D reconstruction method employed here do not produce dark or bright artefact rings around particles and porosities: errors concerning the nature of particles and porosities are therefore excluded.

3.1. *Two-dimensional (2D) and three-dimensional (3D) particles and porosities distributions*

Statistical 3D particle distributions obtained using 320 nm voxel size tomography are presented in Figure 2a. In the plates studied here, Mg_2Si particles are much smaller than either Al_7Cu_2Fe or Al–Cu–Fe–Mn, which have size distributions of the same order of magnitude. The plate in 2050-T8 contains particles Al–Cu–Fe–Mn slightly larger than particles Al_7Cu_2Fe of 7050-T7451. Integrating these distributions gives the total number of particles $> 10\,\mu m$ in both alloys ($\sim 2300/mm^3$ for 2050 plate and $\sim 3400/mm^3$ for 7050 plate), and the volume fraction ($\sim 0.65\%$ for Al–Cu–Fe–Mn, $\sim 0.78\%$ for Al_7Cu_2Fe and $\sim 0.15\%$ for Mg_2Si).

The comparison between the 'real' and 'ideal' two-dimensional distributions of Al_7Cu_2Fe and Al–Cu–Fe–Mn particles on plane RD-ND (Figure 2b) highlights that in the real case (what we actually observe on 2D surfaces) the number of small particles is overestimated and the number of large particles is simultaneously underestimated, compared to the case where particles are assumed not to have complex shapes (ellipsoids).

On reconstructed 3D slices (Figure 1) porosities are visible in both alloys. The maximum size of porosities deduced from the size distribution is about 10 μm equivalent diameter for both plates (Figure 3), and the volume fractions lie near 0.015%. Two-dimensional measurements failed at obtaining a similar distribution on polished surfaces due to their small size (statistically few on a given slice) and the fact that porosities may be filled during polishing. A scanning electron microscope (SEM) image of one particle situated near porosities is obtained in the 2050-T8 plate (Figure 4): one of the porosities is filled.

3.2. *Clustering of particles and porosities*

Results presented here were calculated using a critical distance between particles and porosities of $D = 3$ voxels (0.96 μm). In order to obtain a contact criterion between particles and porosities, D should be as low as possible. During the thresholding of particles and porosities, an error of one or two voxels might appear: a minimum acceptable value is therefore arbitrarily fixed at 3 voxels. Since results are almost identical when increasing D to 6 voxels and 9 voxels, the critical value is kept at 3 voxels.
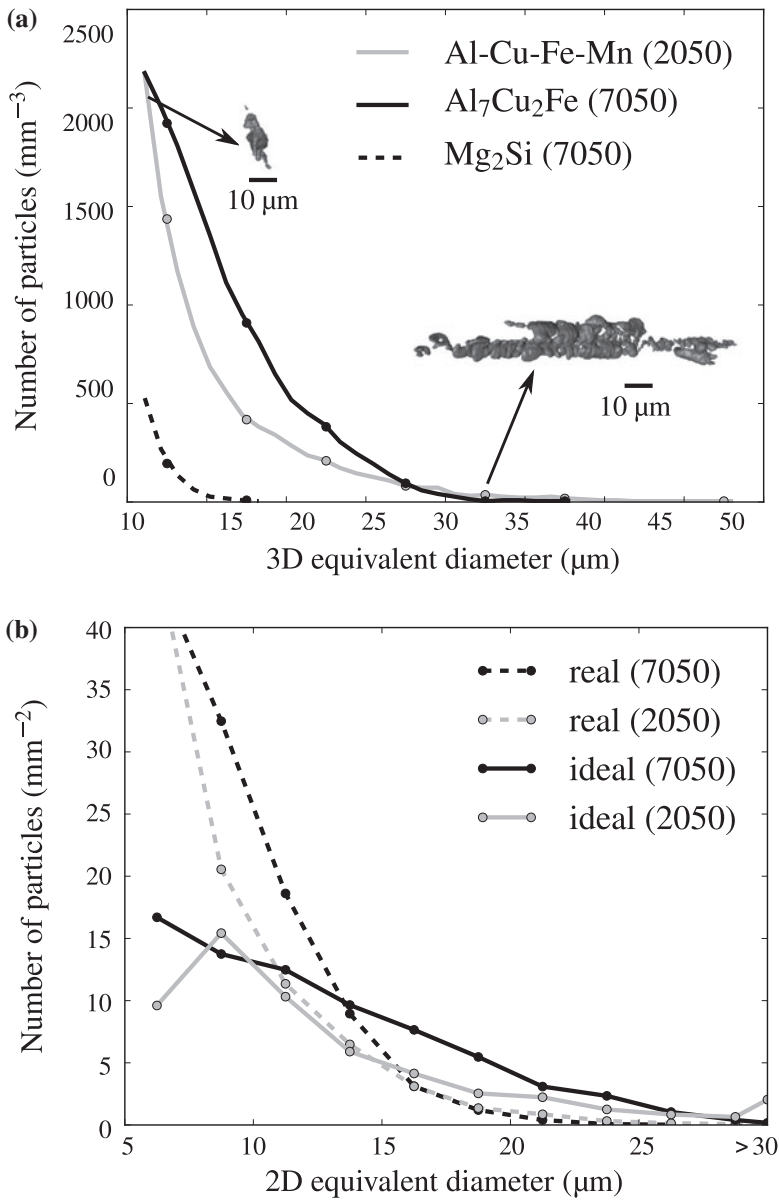
Figure 2. (a) 3D size distribution of Al–Cu–Fe–Mn particles (2050-T8), Al_7Cu_2Fe and Mg_2Si particles (7050-T7451) (plot bin width = $5 \mu m$), (b) comparison between 3D and 2D distributions on RD-ND plane: 'ideal' means that particules are considered as ellipsoids, whereas 'real' refers to image analysis on real slices (plot bin width = $2.5 \mu m$).
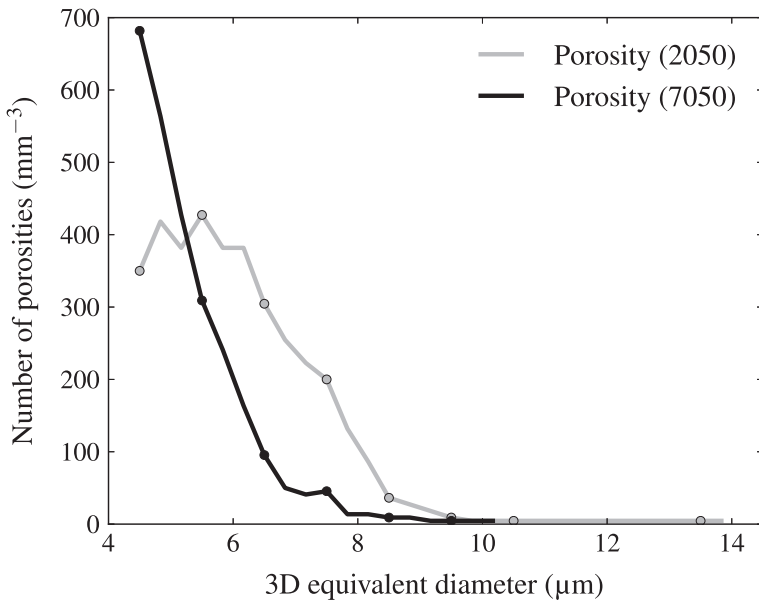
Figure 3.　3D porosities size distribution contained in 2050-T8 and 7050-T7451 plates (plot bin width = 1 µm).
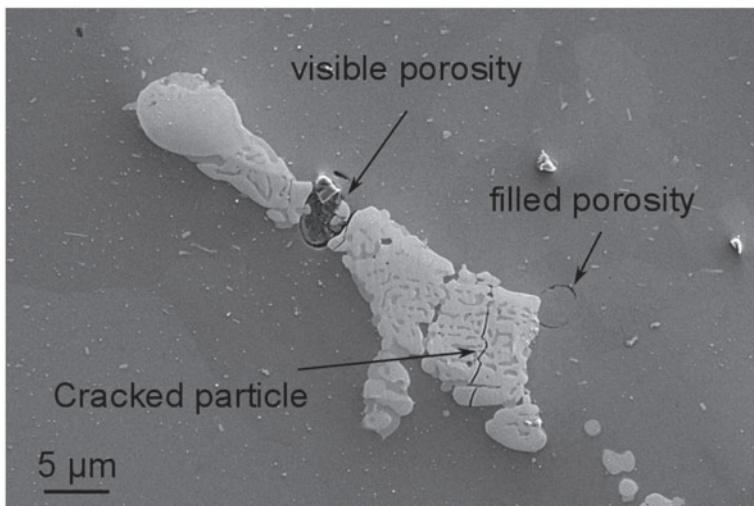

Figure 4.　(2050-T8 plate) SEM-SE micrograph of an Al–Cu–Fe–Mn particle. A porosity is visible in the centre of the particle, but due to polishing some are almost not distinguishable (dark circle reveals a filled porosity).

Using the algorithm described in § 2.3, three main results concerning particles and small porosities clusters are obtained (Figure 5):

(1) First, for clusters containing both particles and porosities, the larger the cluster (*i.e.* the particles), the larger the porosities inside (Figure 5b).

(2) Second, the larger the cluster, the higher the probability that it contains a porosity. When considering porosities larger than 4 μm (mean position of the peak in the 3D porosities size distribution in 2050-T8 and 7050-T7451 plates) the probability is larger than 50% for clusters larger than 20 μm, and reaches almost 100% for clusters larger than 35 μm. The probability is slightly higher in 2050 plate compared to 7050 plate (Figure 5a).

(3) Third, the larger the porosity, the higher the probability that it lies in a cluster. When considering particles larger than 15 μm (three times the critical size for fatigue initiation reported in the literature [7,25]) the probability is larger than 50% for porosities larger than 6 μm, and is almost 100% for those larger than 10 μm. The results are very similar in both alloys (Figure 5c).

In this analysis, it is shown that large particles are most of the time in contact with porosity. This point will be discussed later, since the larger particles are more likely to initiate fatigue cracks in the studied plates as well as in similar aluminium alloys [25,26].

4. 50 nm voxel size magnified holotomography: results

The previous section detailed information that can be obtained with high-resolution tomography. We now focus on holotomography with voxel size 50 nm.

4.1. *Particle cracking*

Using phase contrast in holotomography, it is possible to visually distinguish cracked and non-cracked particles (Figure 6), as already observed by Requena et al. [14] on a SiC particle contained in the 2124/SiC/25p metal matrix composite. The studied volume is small ($8.4 \cdot 10^{-4}$ mm^3), so that only a small number of particles is analysed here. In the 2050-T8 plate, two Al–Cu–Fe–Mn particles are cracked: both of them are in contact with porosity, and the crack in the particle is connected with the porosity (visualization on Figure 7, left). A last porosity is observed, which separates a particle in two independent parts: it could be considered itself as a crack. For the plate in 7050-T7451, three cracked Mg_2Si particles – which are known to fracture easily [27] – are identified, and no Al_7Cu_2Fe. For two of the cracked Mg_2Si, no porosity is observed in their vicinity. For the third one, two porosities are in contact with the particle, however, they are not connected with the cracks in it. A last porosity is situated near a non-cracked Al_7Cu_2Fe particle (Figure 7, right).

Error bars representing effective 80% confidence interval (taking into account the number of particles studied) are calculated [28]. From these observations, it is possible to plot the fraction of cracked particles prior to loading *vs* the 3D equivalent diameter. Two conclusions can be drawn (Figure 8): (i) the cracking probability during the process is different depending on the type of particle (Mg_2Si, Al_7Cu_2Fe, Al–Cu–Fe–Mn), (ii) large particles are more likely to be cracked.
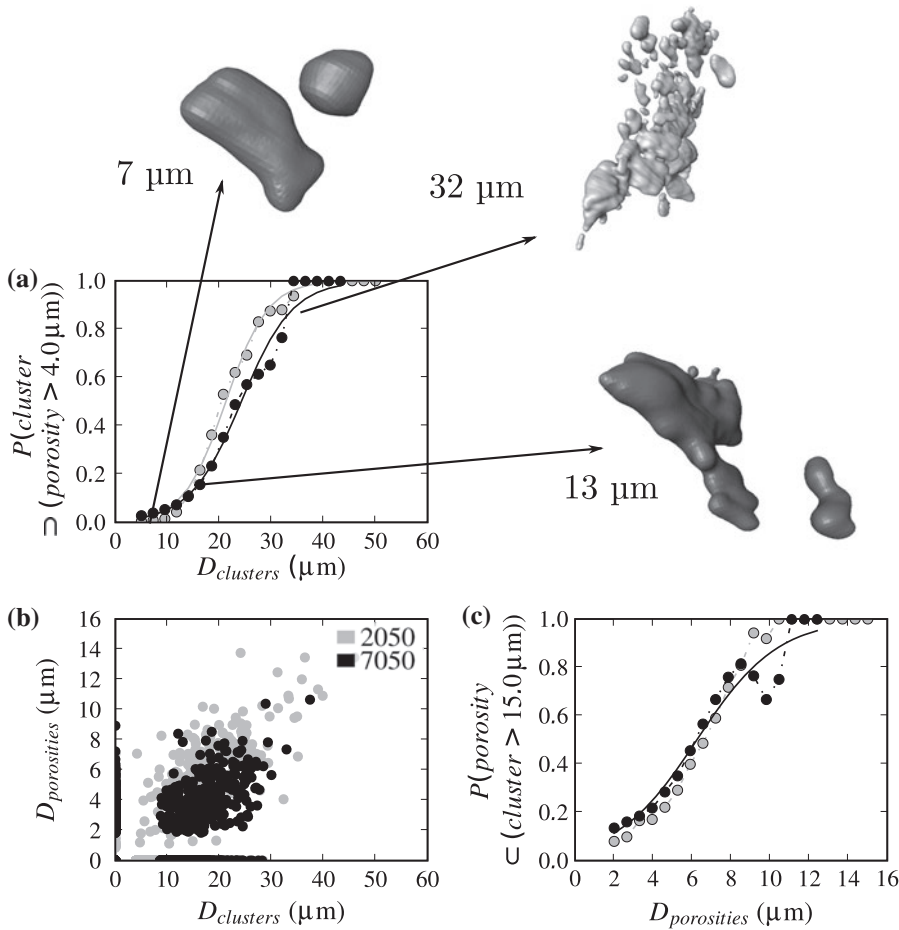
Figure 5. (a) Probability for a large particle to contain a porosity, and Al–Cu–Fe–Mn particles visualization from the 2050-T8 plate, (b) Size of porosities relative to the cluster size it is contained in, (c) Probability for a porosity to lie near a large particle.

4.2. *Particle density measured with holotomography*

On Figure 9, grey levels corresponding to the peaks maximums are associated with particles. As in Section 2.3.1, the peak of voxels with a grey level lower than the grey level of the matrix is associated with Cu-rich particles. In the 7050-T7451 plate, the peak with a higher grey level is associated with Mg_2Si particles. Applying the formula from Equation 1 to the light grey particles in the 7050 plate provides a mass density of 2.09. The error due to the assumption that electron density is proportional to weight density is expected below $\pm 7\%$ (see appendix). The real density measured for Mg_2Si is 1.99 [29]. For dark particles in the 7050 plate, a density of 4.25 has been found, which should be compared to the value 4.30 measured by Bown and Brown [30] for Al_7Cu_2Fe particles. Therefore, measurements
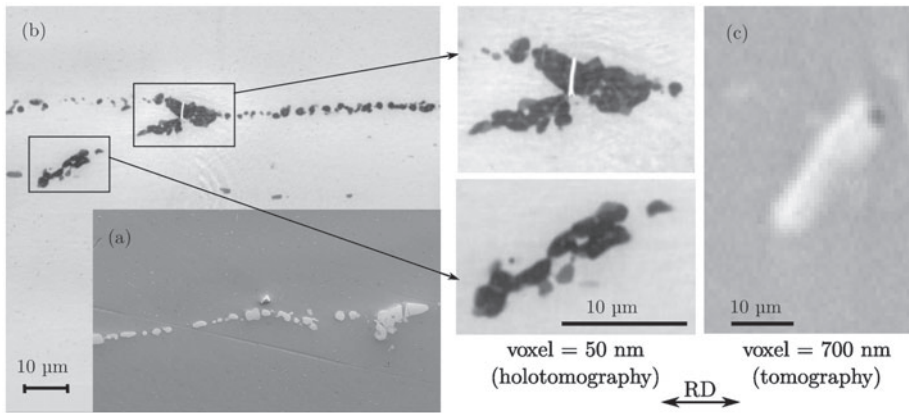
Figure 6. Comparison of images in RD-TD plane (2050-T8 plate) between (a) SEM-secondary electrons imaging, (b) a slice obtained with the holotomography technique (inversed colours: particles are in dark) and (c) a slice obtained with high-resolution tomograraphy.
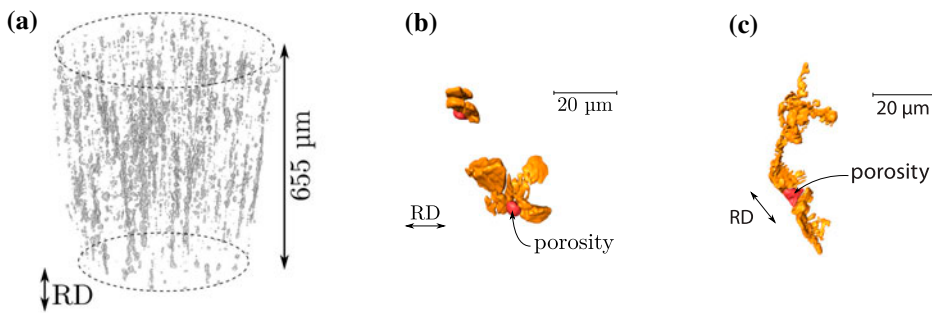

Figure 7. (colour online) 3D surface visualization of particles (grey/orange) and porosities (red) with high-resolution (a) and nanoresolution (b and c). On (b), a crack in the particle begins at the porosity.

displayed in Table 2 can be considered with a precision better than 10%. Applying the formula to Cu-bearing particles in the 2050-T8 plate, which properties are unknown, shows that their density is similar to that obtained for Al_7Cu_2Fe.

5. Discussion

In this study, the smallest diameters considered for particles and porosities are around $3\,\mu m$. Since for a voxel of $0.32\,\mu m$ the resolution lies empirically near $0.64\,\mu m$, high-resolution tomography appears to be adapted for the present statistical analysis: while lower resolution would not have been sufficient, higher resolution would imply a too small
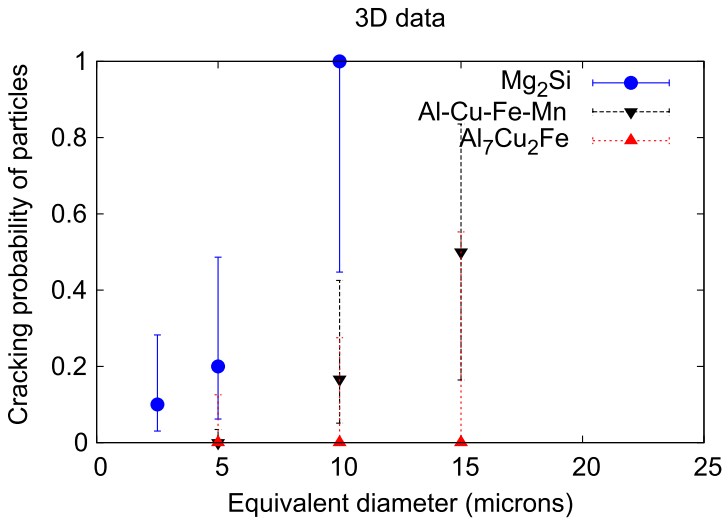
Figure 8. (colour online) Cracking probability of particles in as-received 2050-T8 and 7050-T7451 plates with respect to their nature and 3D equivalent diameter (80% Wilson's confidence interval [28]).

Table 2. Comparison of density measured in the literature ($d_{measured}$) [29,30], calculated thanks to lattice parameters ($d_{calculated}$), and measured using holotomography grey-levels ($d_{holotomo}$).

Phase	Matrix 2050	Matrix 7050	Cu-rich Al–Cu–Fe–Mn	Al_7Cu_2Fe	Mg_2Si	porosity 2050	porosity 7050
$d_{measured}$	2.71	2.83	–	4.30 ± 0.08	1.99	0	0
$d_{calculated}$	–	–	–	4.10 ($a = 0.64$, $b = 1.48$)	2.0 ($a = 0.635$)	0	0
Grey level (32-bits)	−3	−3	−444	−417	212	752	823
$d_{holotomo}$	–	–	4.29 ± 0.43	4.25 ± 0.43	2.09 ± 0.21	–	–

analysed volume (*i.e.* less representativity). On the other hand, holotomography allows to analyse very precisely a small number of particles and porosities.

We discuss here the data obtained with high-resolution and 50 nm voxel size magnified holotomography, regarding fatigue properties.

At the macroscopic level, 2D particle distributions (sometimes only extreme value distributions) are classically used to compare alloys and are sometimes used in mathematical models to predict fatigue lifetime [31]. Though, the measured 2D distributions have been now experimentally shown to underestimate the number/size of large particles (Figure 2), which are the most relevant for the study of fatigue crack initiation. This is attributed to the fact that large particles with 3D complex shapes might be considered as many small ones with 2D observations. Thus, when 2D distributions of particles from different plates
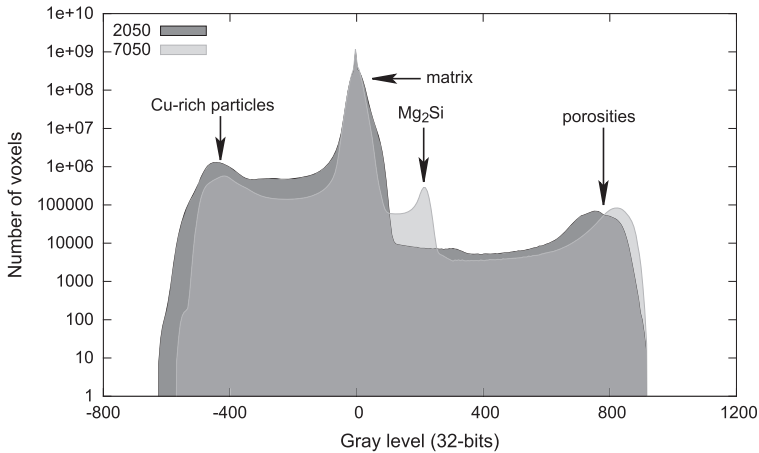
Figure 9. Grey level distribution in reconstructed volumes of 2050-T8 and 7050-T7451 specimens. Peaks positions are quantitatively related to particles densities.

are compared, it should be verified or assumed that the bias introduced by 2D observations is the same. The bias induced by the complex shape of particles is significant in both alloys in RD-ND plane, therefore, retrieving 3D distributions from 2D ones should be done carefully. In this study, 3D distributions of particles are directly measured for both alloys, which provide reliable data.

At the microscopic level, fatigue crack initiation on flat surfaces in commercial alloys may happen to be related with local stress concentration risers as cracked particles, or large porosities [31].

In the literature, the role of cracked particles on fatigue crack initiation in rolled aluminium alloys is shown to be important [6,32], including for the studied plates [33]. In these studies, some particles are cracked in as-received plates, and other may crack during mechanical loading. This paper shows that particles of both plates may be cracked in the as-received volume (Figure 6), and the probability of cracking increases with their 3D size and depends on their type (Mg_2Si, Al_7Cu_2Fe, Al–Cu–Fe–Mn) (Figure 8). This 3D analysis completes those of the literature which are only on 2D polished surfaces [6,33], and both results (dependence on size and type) are consistent with them. It should be noticed that cracked particles detected with the nanotomography technique could not be observed with a SEM in this study: nanotomography provided a 3D image of the inside of the specimen, and thus an extremely high-precision polishing would have been required for SEM sample preparation. No direct comparison of cracked particles images by SEM and nanotomography is therefore available yet, either here or in the literature.

Since the type of particles has an influence on the propensity of cracking, their properties are very important, while difficult to access. One of them, the density, has been obtained with holotomography in the present study. It has been shown that despite their different cracking probability Al–Cu–Fe–Mn and Al_7Cu_2Fe particles have similar densities.

Small porosities as described in this study were not underlined as effective fatigue crack initiation sites in the literature. Two explanations are proposed: (i) such porosities are less

detrimental than cracked particles, and (ii) they may be located a few microns under the surface investigated.

The proximity of particles and small porosities has not been investigated in the past for such aluminium alloys. In this paper, we show that the larger particles, which are believed to initiate fatigue cracks, are very likely to stay in contact with a small porosity. Even if no significant effect on fatigue initiation has been attributed to small porosities in the literature, the lack of 3D experiments may hide their role, which might be coupled with that of particles. The fact that cracks in all three Al–Cu–Fe–Mn particles observed with holotomography start at porosities could indicate that, for Al–Cu–Fe–Mn particles in the 2050-T8 plate, the presence of porosities could be correlated with particle cracking.

6. Summary

High-resolution tomography provided particle and porosity size distributions and showed that porosities are statistically located near large particles. The error made on 2D distributions obtained on surfaces has been quantified. A voxel size of 320 nm is identified as an appropriate resolution for 3D statistical studies of the distribution/cluster of particles and porosities, which are involved in fatigue crack mechanisms in 2050-T8 and 7050-T7451 plates.

With *nanoresolution* the proximity of cracked particles and small porosities could be visualized precisely. This provided real 3D data about microscopic stress concentration risers that may lead to fatigue crack initiation: mesh can be extracted and further used in finite element analysis. Nanoresolution tomography also enables the measurement of microscopic particles densities.

Disclosure statement

No potential conflict of interest was reported by the authors.

References

[1] J.C. Grosskreutz and G.G. Shaw, *Critical mechanisms in the development of fatigue cracks in 2024–T4 aluminium*, in *Fracture 1969*, P.L. Pratt, ed., Chapman & Hall, Brighton, 1969, pp. 620–629.
[2] S. Pearson, Eng. Fract. Mech. 7 (1975) p.235.
[3] S. Suresh, *Fatigue of Materials*, Cambridge University Press, Cambridge, 1998.
[4] L. Farcy, C. Carre, M. Clavel, Y. Barbaux and D. Aliaga, J. Phys. Colloq. 48 (1987) p.3.

[5] T. Sanders and J.T. Staley, *Review of fatigue and fracture research on high-strength aluminium alloys*, in *Fatigue and Microstructure*, M. Meshii, ed., ASM, Metals Park, Ohio, 1978, pp. 467–516.

[6] J. Payne, G. Welsh, R.J. Christ, J. Nardiello and J.M. Papazian, Int. J. Fatigue 32 (2010) p.247.

[7] W. Wen, A.H. Ngan, Y. Zhang, B. Xu and T. Zhai, Mater. Sci. Eng. A 564 (2013) p.97.

[8] J. Delacroix, *Etude des mecanismes de fissuration en fatigue et/ou fretting d'alliages Al-Cu-Li* [Effects of microstructure on the incipient fatigue and/or fretting crack processes in Al-Cu-Li alloys], Ph.D. thesis, INSA Lyon, 2011.

[9] S. Birosca, J.Y. Buffiere, F.A. Garcia-Pastor, M. Karadge, L. Babout and M. Preuss, Acta Mater. 57 (2009) p.5834.

[10] A. King, W. Ludwig, M. Herbig, J.-Y. Buffiere, A.A. Khan, N. Stevens and T.J. Marrow, Acta Mater. 59 (2011) p.6761.

[11] H. Proudhon, A. Moffat, I. Sinclair and J.-Y. Buffiere, C.R. Phys. 13 (2012) p.316.

[12] L. Laiarinandrasana, T.F. Morgeneyer, H. Proudhon, F. N'guyen and E. Maire, Macromolecules 45 (2012) p.4658.

[13] R. Mokso, P. Cloetens, E. Maire, W. Ludwig and J.-Y. Buffiere, Appl. Phys. Lett. 90 (2007) p.144104.

[14] G. Requena, P. Cloetens, W. Altendorfer, C. Poletti, D. Tolnai, F. Warchomicka and H.P. Degischer, Scr. Mater. 61 (2009) p.760.

[15] D. Tolnai, G. Requena, P. Cloetens, J. Lendvai and H.P. Degischer, Mater. Sci. Eng. A 550 (2012) p.214.

[16] Y. Ma, X. Zhou, G.E. Thompson, T. Hashimoto, P. Thomson and M. Fowles, Mater. Chem. Phys. 126 (2011) p.46.

[17] W.L. Morris, Metall. Mater. Trans. A 9A (1978) p.1345.

[18] Y. Xue, H. El Kadiri, M.F. Horstemeyer, J. Jordon and H. Weiland, Acta Mater. 55 (2007) p.1975.

[19] E. Maire, N. Gimenez, V. Sauvant-Moynot and H. Sautereau, Philos. Trans. R. Soc. A 364 (2006) p.69.

[20] J.-H. Han and D.-Y. Kim, Acta Metall. Mater. 43 (1995) p.3185.

[21] R.L. Fullman, Trans. AIME 197 (1953) p.447.

[22] N. Limodin, L. Salvo, M. Suéry and F. Delannay, Scr. Mater. 60 (2009) p.325.

[23] J. Russ and R. Dehoff, *Practical Stereology*, Plenum Press, New York, 1999.

[24] P. Cloetens, W. Ludwig, J. Baruchel, D. Van Dyck, J. Van Landuyt, J. Guigay and M. Schlenker, Appl. Phys. Lett. 75 (1999) p.2912.

[25] P.J. Laz and B.M. Hillberry, Int. J. Fatigue 20 (1998) p.263.

[26] C.Y. Kung and M.E. Fine, Metall. Mater. Trans. A 10 (1979) p.603.

[27] Y. Shen, T.F. Morgeneyer, J. Garnier, L. Allais, L. Helfen and J. Crépin, Acta Mater. 61 (2013) p.2571.

[28] A. Agresti and B.A. Coull, Am. Stat. 52 (1998) p.119.

[29] E.E. Schmid, K. von Oldenburg and G. Frommeyer, Z. Metallkd. 81 (1990) p.809.

[30] M.G. Bown and P.J. Brown, Acta Crystallogr. 9 (1956) p.911.

[31] Y. Murakami, *Metal Fatigue: Effects of Small Defects and Nonmetallic Inclusions*, 1st ed., Elsevier, Oxford, 2002.

[32] J.E. Bozek, J.D. Hochhalter, M.G. Veilleux, M. Liu, G. Heber, S.D. Sintay, A.D. Rollett, D.J. Littlewood, A.M. Maniatty and H. Weiland, Modell. Simul. Mater. Sci. Eng. 16 (2008) p.065007.

[33] E. Nizery, J.Y. Buffiere, H. Proudhon, A. Daniélou and S. Forest, Mater. Sci. Forum 794–796 (2014) p.296.

Appendix 1. Proportionality between number of electrons and weight of atoms

The chemical elements present in both alloys and in the particles studied in this paper are mainly: Al, Cu, Mg, Zn, Li, Mn, Ag, Zr, Fe and Si. As shown in Figure A1, the number of nucleons can be estimated from the number of electrons by the mean of a linear approximation. Values used for chemical elements are those reported in periodic tables. The error induced by such an approximation is below $\pm 7\%$.
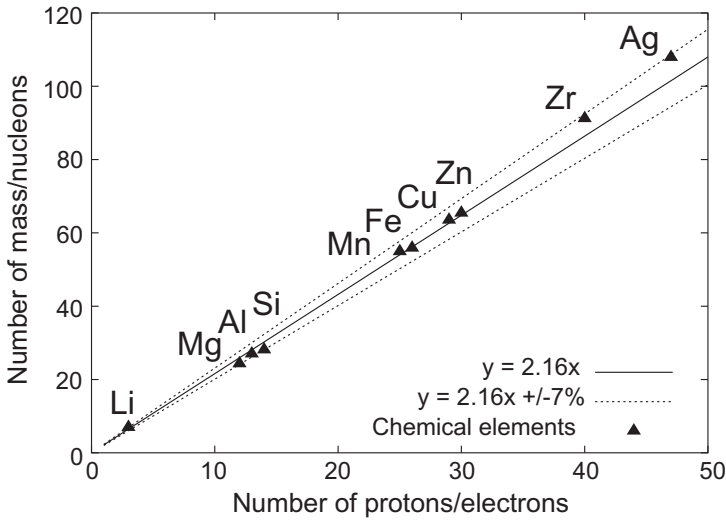

Figure A1.   The number of mass of an atom is correlated with its number of electrons. For the elements contained in the studied alloys, the linear approximation $y = 2.16x$ provides an error of less than $\pm 7\%$.